



Nanoscale

Molecular Self-assembled Monolayers Anomalously Enhance Thermal Conductance across Polymer-Semiconductor Interfaces

Journal:	<i>Nanoscale</i>
Manuscript ID	NR-ART-09-2022-004936.R1
Article Type:	Paper
Date Submitted by the Author:	14-Nov-2022
Complete List of Authors:	He, Jinlong; University of Connecticut Tao, Lei; University of Connecticut Xian, Weikang; University of Wisconsin-Madison, Mechanical Engineering Arbaugh, Tom; Wesleyan University Li, Ying; University of Wisconsin-Madison, Mechanical Engineering; University of Wisconsin-Madison

SCHOLARONE™
Manuscripts

Molecular Self-assembled Monolayers Anomalously Enhance Thermal Conductance across Polymer-Semiconductor Interfaces

Jinlong He ^{a†}, Lei Tao ^{b†}, Weikang Xian ^a, Tom Arbaugh^c and Ying Li ^{a*}

^a *Department of Mechanical Engineering, University of Wisconsin-Madison, Madison, Wisconsin 53706 - 1572, United States*

^b *Department of Mechanical Engineering, University of Connecticut, Storrs, Connecticut 06269 - 3139, United States*

^c *Department of Physics, Wesleyan University, Middletown, Connecticut 06459, United States*

[†] Equal contribution

* Corresponding Author: Email: yli2562@wisc.edu; Phone: +1-608 265 0577; Fax: +1-608 890

3966

ABSTRACT: Thermal issues become increasingly important for the performance and lifetime of highly miniaturized and integrated devices. However, the high thermal resistance across the polymer/semiconductor interface greatly weakens the fast heat dissipation. In this study, applying the self-assembled monolayers (SAMs) technique, organic molecules are employed as heat regulators to mediate interfacial thermal conductance (ITC) between semiconductors (silicon, or Si) and polymer (polystyrene or PS). Silane-based SAMs molecules with unique functional groups, such as $-NH_2$, $-CH_3$, $-SH$, and $-Cl$, are orderly assembled into Si-PS interfaces. Their roles in ITC and heat transfer mechanism were systematically investigated. Molecular simulations demonstrate that the Si-PS interface decorated with SAMs molecules can significantly facilitate heat transfer in varying degrees. Such difference is primarily due to the different non-bonded interactions and compatibility between SAM and PS. Compared with the pristine Si-PS interface, the interface incorporated with 3-chloropropyl trimethoxysilane shows the greatest improvement on ITC, about 507.02%. Such improvements are largely attributed to the SAM molecules, as the thermal bridges straighten molecular SAM chains, develop strong non-bonded interactions with PS, provide the covalent bonding between Si and PS, present the strong coupling effect between two materials' vibrational modes, and eliminate the discontinuities in the temperature field. Eventually, these demonstrations are expected to offer molecular insights to enable effective thermal management through surface engineering for critical-heat transfer materials and microelectronic devices.

KEYWORDS: polymer/semiconductor nanocomposites, molecular engineering, interfacial thermal conductance, self-assembled monolayers, molecular dynamics

1. Introduction

The development of microelectronic devices has promoted the growth of many industries like self-driving cars, wearable electronics, and telecommunications. As modern microelectronic devices are highly integrated systems of different materials, the reliability of the system becomes a critical challenge, such as the overheating problem [1-4]. Since the thermal transport within microelectronic devices is mostly hindered by the low interfacial thermal conductance (ITC) between dissimilar materials or layered materials, how to improve ITC turns into the key, and it has been studied widely for many years [5-9]. Especially, when polymers are employed in microelectronics devices, their relatively low thermal conductivities bring in a significantly low ITC issue [10-12]. Therefore, a careful design of the interface is vital for a hybrid system to achieve good interfacial thermal transport [13-15].

Various methods can be used to improve the ITC. Introducing a self-assembled monolayer (SAM) is one effective way to reduce the thermal resistance between dissimilar materials [16-24]. For example, Song et al. [25] investigated the polyethylene glycol (PEG)-gold interface. They found that increasing SAM angle value from 100° to 150° led to PEG penetrating into SAM chains, which led to a significantly increased ITC. Zheng et al. [26] demonstrated that the ITC could be greatly enhanced by incorporating the SAMs between sapphire and polystyrene. Additionally, Zhang et al. [27] paid attention to how hydrogen bonds (H-bonds) contribute to thermal transport across various interfaces, such as between gold and four organic liquid materials including hexanol, hexane, hexanamine, and hexanoic acid. When the gold surface was functionalized by three distinct SAM molecules, such as 1-hexanethiol, 6-mercaptohexanoic acid, and 6-mercapto-1-hexanol, they found the formed H-bonds could effectively improve interfacial thermal transport. Moreover, concerning the interfaces of polymers and semiconductors, Zhang et al. [28, 29]

demonstrated that polyethylene and poly(vinyl alcohol) SAM could improve the ITC of graphene and poly(methyl methacrylate) dramatically. Lu et al. [30] utilized polyethylene-SAM molecules to decorate the polystyrene-silicon interface and focused on the effects of the packing density and length of SAM alkyl chains on ITC. They discovered that high ITC could be obtained via high SAM density or moderate packing density plus with 6-8 carbons along the SAM alkyl chains. Xu et al. [24] studied that the existing H-bonds at the silica-water interface can offer more bridges for thermal conduction and speed up the ITC.

Although many SAM studies have been reported to enhance the ITC of soft-hard material systems, it is difficult to identify a universal mechanism to explain how different SAMs affect ITC on different systems. When polymers are interfacing with conductors, insulators, and semiconductors, their ITC performance and the controlling mechanism are system-dependent; namely, a case-by-case analysis is required when carrying out ITC analysis. With the experiences obtained from the aforementioned studies, it is realized that various characteristics of SAMs are important in determining the ITC, such as the length of SAMs [31], the distinct functional groups in SAMs [28, 32], and the backbone length of SAMs [33], etc. To particularly address the thermal transport of polymer-semiconductors systems that are not fully investigated, this study focuses on a polystyrene (PS)-Si system and demonstrates the effect of SAMs on its ITC and how heat flux was transferred across the Si-PS interfaces after the introduction of SAMs.

To mediate the ITC between Si and PS, we assemble silane-based SAM molecules into the interface to form the Si: SAMs-PS system. Next, we investigate the effect of different SAM molecules having different functional groups on ITC, such as $-NH_2$, $-SH$, $-CH_3$, and $-Cl$. Our molecular simulation results indicate that the grafted SAM molecules can efficiently improve the ITC between Si and PS. To further understand how the functional SAM molecules influence the

ITC, we systematically illustrate their heat transfer mechanisms on the interface. The non-bonded interactions between the PS and SAM molecules, the extended molecular morphology, the covalent bonding between Si and PS, and the coupled vibrational modes of two materials, etc., are revealed to significantly contribute to the improved ITC. These findings provide physical insights into the mechanism of the improved ITC at the atomic level, which is a valuable guideline for a more effective thermal management on highly integrated microelectronic devices.

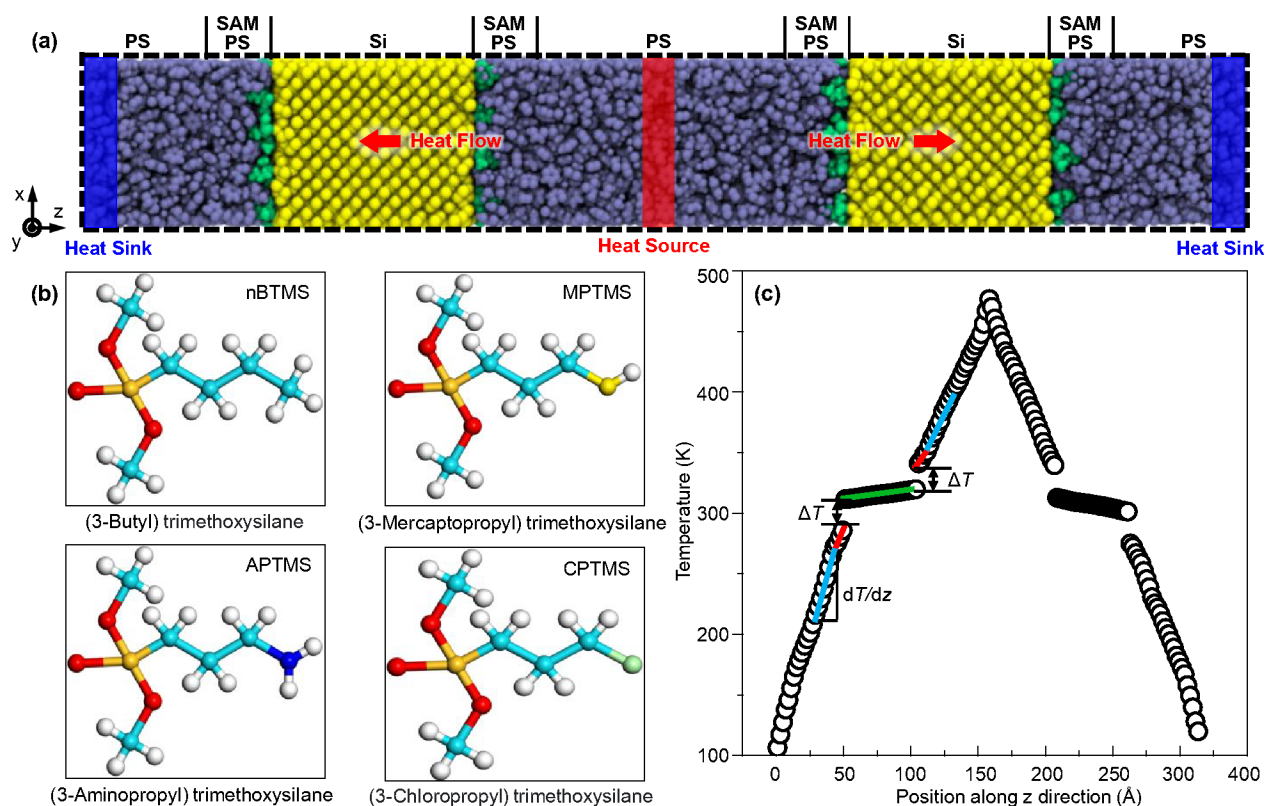


Fig. 1. (a) An all-atom simulation setup for calculating the ITC between PS and Si through the reverse non-equilibrium molecular dynamics (RNEMD) simulations with periodic boundary conditions (PBCs) imposed on three (x , y , and z) directions. (b) Four organic molecules are selected as the thermal bridges, including 3-Butyl trimethoxysilane (nBTMS), 3-Mercaptopropyl trimethoxysilane (MPTMS), 3-Aminopropyl trimethoxysilane (APTMS), and 3-Chloropropyl trimethoxysilane (CPTMS). (c) A typical temperature profile generated by RNEMD simulations. Here, the dropped temperature across Si/PS interface is shown as ΔT , and the temperature gradient within the PS matrix is denoted as dT/dz .

2. Atomistic Models and Computational Methods

2.1. Atomistic Models for Polymer-Semiconductor Interfaces

Fig. 1a presents a typical atomistic heat-transfer model with multiple polymer-semiconductor (PS-Si) interfaces. Silicon crystal has a cross-section of $43.44 \text{ \AA} \times 43.44 \text{ \AA}$. The unit cell geometry for the Si crystal is displayed in **Fig. S1**, which is a cubic crystal with a length of 5.43 \AA along all sides. As shown in **Fig. 1b**, four SAMs molecules were employed to graft on the Si surface, including 3-butyl trimethoxysilane (nBTMS, or $-\text{OSi}(\text{OCH}_3)_2(\text{CH}_2)_3\text{CH}_3$), 3-mercaptopropyl trimethoxysilane (MPTMS, or $-\text{OSi}(\text{OCH}_3)_2(\text{CH}_2)_3\text{SH}$), 3-aminopropyl trimethoxysilane (APTMS, or $-\text{OSi}(\text{OCH}_3)_2(\text{CH}_2)_3\text{NH}_2$), 3-chloropropyl trimethoxysilane (CPTMS, or $-\text{OSi}(\text{OCH}_3)_2(\text{CH}_2)_3\text{Cl}$). These four SAM molecules almost have the same backbone length but unique end groups. All SAM molecules were covalently and evenly assembled into the Si surface. Using the Monte Carlo-based self-avoiding random walk approach [34], the initial PS configuration was built with 40 repeat units in each polymer chain. Both SAM molecules and Si were constructed through our in-house codes. All material components, such as Si, SAM molecules, and PS, were entirely equilibrated first prior to being combined into VMD [35] to form the integrated Si-PS interface model. The grafted SAMs molecules and PS polymer contact with the xy -plane ([001]) of Si crystal. The cross-section size normal to the heat flux direction (z -direction) was constructed large enough to avoid the influence of the lateral size on ITC [36-39]. Studies on the $\alpha\text{-Fe}_2\text{O}_3$ crystal and the organic-inorganic interface have indicated the lateral size of 35 \AA is sufficient to cover all the dominant phonon modes contributing to the ITC [36, 39], leading to a converged thermal conductance. Periodic boundary conditions (PBCs) were exerted in all directions (x , y , and z).

2.2. *Molecular Dynamics Simulations*

All molecular dynamics (MD) simulations were conducted using the Large-scale Atomic/Molecular Massively Parallel Simulator (LAMMPS) package [40]. The Si-Si interactions were modeled using Tersoff potential [41]. The OPLS-AA potential parameters [42, 43] were used to describe PS and SAM molecules, which have been extensively employed to simulate organic materials and their interfaces [44, 45]. The optimized universal force field (UFF) parameters are used to describe the interfacial adhesion between Si and polymers through non-bonded interactions [32, 46]. Conjugate gradient algorithm-based energy minimization was first performed for initial structures, followed by relaxing the system in the NPT ensemble (1.0 atm and 300 K) over 2 ns, and then transferring to the NVT ensemble (300 K) with 2 ns. 5 annealing cycles continue to be performed to eliminate thermal residual stresses. During each annealing process, the system temperature was first raised from 300 K to 500 K within 2 ns, then relaxed over 1 ns at 500 K, and finally dropped down to 300 K within 2 ns. Next, the system was relaxed for over 2 ns within the NPT ensemble (1.0 atm and 300 K), followed by a relaxation time of 2 ns in the NVT ensemble (300 K). The time step for equilibrium runs was set up to 1.0 fs, and a reduced 0.5 fs for the successive production runs. Before performing production simulations, the system was further equilibrated for another 5 ns again within the NVT ensemble (300 K), employing a smaller time integration step of 0.5 fs. The special production times are described in detail in each of the following method parts and also summarized in **Table S1**. To remove the statistical randomness, five different initial configurations, each considering six different initial velocities for each simulation system (thirty simulations in total for each system), are employed to carry out all the following simulations.

2.3. *Thermal Conductance across Polymer-Semiconductor Interface*

The reverse non-equilibrium molecular dynamics (RNEMD) approach [47, 48] was implemented to analyze the thermal conductance across the Si-PS interface using the simulation system shown in **Fig. 1a**. Numerically enforcing a heat flux through atomic velocity exchanging, ITC between the PS and Si interface was calculated using the expression of $G = J \Delta T^{-1}$, where ΔT defines the fallen temperature across the interface (**Fig. 1c**) and J is the heat flux. In this work, along the heat flow direction (z -direction in **Fig. 1a**) each simulation system was uniformly separated into 156 slabs. The heat gradient was developed by exchanging the highest energies in the blue region (heat sink) with the lowest energies in the red region (heat source). When carrying out the velocity exchange, a virtual elastic collision was exerted to keep the system's momentum and energy conservation. After the system reaches a steady state, the calculated heat flux could be written using $J = \Delta E (2tA)^{-1}$. Here, ΔE defines the exchanged energy within each swap, A denotes the system's cross-sectional area, t represents the time period between velocity swaps, and the constant "2" is responsible for two symmetric routes in heat conduction. Using the RNEMD sampled data over 20 ns, thermal conductance across the Si-PS interface was then calculated after the system is in a steady state. As displayed in **Fig. 1c**, the temperature gradient profile was counted by assessing all slabs' average temperature. Based on the obtained temperature profile, the dropped interfacial temperature (ΔT) between Si and PS was calculated. J together with ΔT provides G . Beyond that, the simulation system can also provide PS thermal conductivity, defined by $K = (dT/dz)^{-1} J$. Here, dT/dz gives the changed temperature gradient within the PS matrix (red lines in **Fig. 1c**). To demonstrate RNEMD calculations, non-equilibrium molecular dynamics (NEMD) simulations were also employed as an additional method to evaluating G . On one hand, half of the system employed in the RNEMD simulation (**Fig. 1a** and **Fig. S2a**) was adopted for NEMD. On the other hand, the source's temperature was fastened at 335 K for NEMD, while the sink's

temperature was moderated to meet the interfacial temperature of around 300 K. **Fig. S2b** shows a typical temperature profile calculated by NEMD simulations. Using a time integration step of 0.5 fs, both RNEMD and NEMD simulations were carried out with a production run of 20 ns. The final ITC for each simulation system was obtained by averaging thirty independent simulations.

2.4. Temperature Distribution and Density Profile

NEMD simulations were conducted to assess the whole system's temperature contours. Temperatures were fastened at 250 K and 450 K for the sink region and the source region, respectively, as shown in **Fig. S3**. Two boundaries (black color) are fixed by 1 Å along the z -direction and excluded their interactions for all calculations. Besides, to prevent heat leakage caused by PBC along the z -direction, two 10 Å thick vacuum layers (on both two sides) next to the two fixed areas are assigned. Each model within the y - z plane was first equally sectioned into 80×600 cells. The total dimensions are 43.44 Å and 150 Å along the y - and z -direction, respectively. The z -cell size is chosen as a small enough length of 0.25 Å, and each cell can only contain PE polymer or Si atoms. Then, each divided cell has a size of $0.543 \text{ Å} \times 0.25 \text{ Å}$ along the y - z plane. Atoms are allocated into these divided cells according to their y and z positions at each time step. When the steady state was achieved, atomic velocities and positions were then reported during a simulation interval of 5 ns. The temperature profiles were calculated by averaging the temperature related to all reported atoms inside each cell. The atomic number density profiles were analyzed by calculating all atoms in each cell. In addition to that, a temperature of zero gives the cells where no atoms are present.

2.5. Autocorrelation Function of Interfacial Heat Flow

According to the Green-Kubo theory [49], i.e., $\int_0^\infty \langle H(0) \cdot H(t) \rangle dt$, where $H(t)$ represents the swapped heat flux between two materials at time t , e.g., PS polymer and the filler materials

denoted by P_{Filler} , the ITC is proportion to the autocorrelation function of interfacial heat flow.

$H(t)$ was expressed as $H(t) = \sum_{j \in P_{Filler}} \vec{F}_{ij} \cdot \vec{v}_i - \sum_{j \in P_{Filler}} \vec{F}_{ji} \cdot \vec{v}_j$. Here, \vec{v}_i defines the velocity

vector, and \vec{F}_{ij} represents the force vector that atom j imposes on atom i . The system is performed at equilibrium over 20 ns production run with an autocorrelation time of 40 ps.

2.6. Interfacial Adhesion between Two Materials

The interfacial adhesion between PS and the modified Si was evaluated using NEMD to pull out the functionalized Si from PS. As shown in **Figure S4**, only a part of the well-equilibrated system was employed. All atoms within the region at the left “P1” plane were fastened. All atoms located in the right “P2” plane were treated as rigid. Using a time integration step of 0.1 fs, the pulling process is carried out under the NVT ensemble (300 K). The driving force is applied to the centroid of the rigid and forces the rigid to move along the z direction with a constant speed (20 m s^{-1}). All atoms between the two planes, “P1” and “P2”, were set to be flexible. As the pulling time increases, the imposed force versus the interfacial separation distance is sampled along the loading direction. The interfacial adhesion was further quantified by integrating the sampled force-displacement curve.

2.7. Miscibility between PS and SAM Molecules

Three interaction parameters, such as Flory-Huggins (χ), mixing energy (E_{mix}), and solubility parameter (δ), is calculated to explore the miscibility between PS and SAM molecules. The Flory-Huggins model employed in this study is based on the mixing thermodynamics in the polymer/polymer and solvent/polymer binary system [50, 51], which is widely applied to analyze the mixture’s free energy in a binary system. In order to analyze E_{mix} , the coordination number, ZZ_{xy} , is first evaluated, which denotes the molecular number of the component y that can be filled

around the component x molecule within the excluded-volume constraints. Based on the Flory-Huggins model, each component occupies a lattice site. Then E_{mix} , is expressed as, $E_{mix} = (ZZ_{xy}\langle E_{xy} \rangle + ZZ_{yx}\langle E_{yx} \rangle - ZZ_{yy}\langle E_{yy} \rangle - ZZ_{xx}\langle E_{xx} \rangle)/2$, where ZZ_{ij} and E_{ij} ($i, j = x, y$) are the coordination number and the binding energy between component i and component j , respectively. $\langle \rangle$ represents the ensemble average. In this study, as shown in **Fig. 1a**, bulk PS polymers on the left side (ice grey) are treated as the first component. Each molecular SAM (**Fig. 1b**) is considered as the second component. For molecules, the E_{mix} are calculated by averaging over an ensemble of molecular configurations. Employing Flory-Huggins model, then the χ parameter is expressed as, $\chi = E_{mix}(RT)^{-1}$. Here, T and R represent the temperature and gas constant, respectively.

The solubility parameter (δ) is usually defined by $\delta = (EV^{-1})^{0.5}$, where V is the solvent's molar volume, and E is the total cohesion energy. Then, the E is reconstructed by summing up all individual energies associated with the Hansen parameters, $E = E_D + E_P + E_H$. By dividing the E by V , we can obtain the square of the total δ by adding up all Hansen components. The expression is written as $\delta^2 = \delta_D^2 + \delta_P^2 + \delta_H^2$. Here, δ_D , δ_P , and δ_H represent the dispersion, hydrogen bonding, and polar cohesion parameter, respectively.

2.8. Local Radial Distribution Function (RDF)

The local RDF, $g(r)$, provides a statistical description of the local atomic packing state and atom density distribution by quantifying the atomic spatial distribution around a reference atom. Intrinsically, RDF represents the probability of existing in an atom at a distance r against a reference atom, expressed by $g(r) = \langle \rho(r) \rangle \rho^{-1}$, where $\langle \rho(r) \rangle$ denotes the average local atomic number density at r , and ρ is the bulk density. $\langle \rho(r) \rangle$ is expressed as $\langle \rho(r) \rangle = dn_r/4\pi r^2 dr$, where dn_r describes the number of atoms within a shell of thickness dr . In addition to that, the radial

atomic number density around a reference atom is also analyzed to describe the density of local packing atoms. In this study, using the simulation system shown in **Fig. 1a** and a grafted density of 1.696 nm^{-2} for SAM molecules, the system was fully equilibrated within the NVT ensemble (300 K) over 10 ns based on the final equilibrium configuration obtained in the MD part (2.2). During the simulation process, 0.5 fs is set as the time step. The configurations over the last 5 ns are recorded to analyze the RDF and radial atomic number density on a time interval of 0.1 ps. As shown in **Fig. 1b**, the C, S, N, and Cl atoms are chosen as the reference atom for each nBTMS, MPTMS, APTMS, and CPTMS molecule, respectively. For each SAM molecule, the accumulated RDF and radial atomic number density are first calculated based on the production runs and the total number of SAM molecules. RDF and radial atomic number density are then obtained by averaging both the total production frames and total SAMs' number. In a similar fashion, the final RDF and radial atomic number density are obtained by averaging the thirty independent simulations of each system.

2.8. Vibrational Density of States (VDOS)

VDOS can demonstrate materials' vibration modes at the atomic level, which can be further employed to analyze their vibration features between two dissimilar materials constituting an interface. Usually, using the velocity autocorrelation function-based Fourier transform, VDOS is expressed as $\text{VDOS}(f) = \int_0^{+\infty} e^{-i2\pi ft} CF_v(t) dt$, where t is autocorrelation time and f defines the frequency. $CF_v(t)$ represents the normalized velocity auto-correlation functions expressed by $CF_v(t) = \langle \vec{v}(0) \cdot \vec{v}(t) \rangle / \langle \vec{v}(0) \cdot \vec{v}(0) \rangle$ where $\vec{v}(t)$ is the atomic velocity at a certain moment t and $\langle \cdot \rangle$ denotes the ensemble average. To eliminate the statistical randomness in MD simulations, the

final VDOS was calculated by averaging the thirty independent simulations. Each simulation is conducted with a total production run of 6.4 ns and 0.5 fs is the used time integration step.

2.9. Accumulated Correlation Factor (ACF)

To quantify the correlation intensity or match degree between two dissimilar materials' vibration modes, the *ACF* could be further described using the truncated frequency (f_c). In other words, the *ACF* can describe the vibration coupling intensity up to a given f_c by integrating the frequency domain from 0 to f_c , which is expressed as, $ACF(f_c) = \int_0^{f_c} VDOS_A(f) \cdot VDOS_B(f) df / \int_0^{\infty} VDOS_A(f) df \cdot \int_0^{\infty} VDOS_B(f) df$. Here, $VDOS_A(f)$ and $VDOS_B(f)$ denote the VDOS of two components including A and B, respectively. A lower $ACF(f_c)$ represents a higher mismatch or a lower match with the vibration frequency up to f_c . When f_c exceeds the highest frequency related to all vibration modes, the $ACF(f_c)$ could be equivalent to the extensively adopted correlation factor [52].

3. Results and Discussion

3.1. Validation of Computational Model and Method

The undecorated Si-PS interface was also modeled to corroborate our MD results against experiments and other similar calculations. First, the PS density was calculated to be about $1.03 \pm 0.02 \text{ g cm}^{-3}$ at the equilibrium state, very close to the experimentally measured value of 1.05 g cm^{-3} [53]. Second, the calculated thermal conductivity for PS polymer was found to be $0.126 \pm 0.013 \text{ W m}^{-1} \text{ K}^{-1}$, which also matches well with the measurements ($0.140 \text{ W m}^{-1} \text{ K}^{-1}$) [54, 55]. Third, the single Si thermal conductivity at room temperature was founded to be about $1.26 \pm 0.04 \text{ W m}^{-1} \text{ K}^{-1}$, which is well in accordance with measurements and other simulation results at the same size

[56-58]. Last, the ITC obtained by the RNEMD across the pristine Si-PS interface was found in almost the same order of magnitude as that bonded with van der Waals interactions, such as Sapphire-PS, Si-PE, and Sapphire-HDPE [59-62].

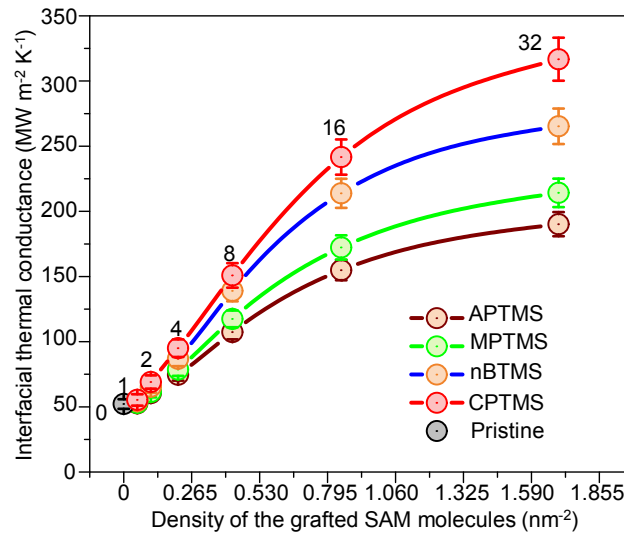


Fig. 2. ITC for the pristine Si-PS interface and four molecular SAM-decorated Si-PS interfaces versus the density of SAM molecules grafted to each side of the Si surface. The numbers of the grafted SAM molecules corresponding to their grafted densities are also marked on the curve.

3.2. Functional Group Dependent Interfacial Thermal Conductance.

Fig. 2 plots the calculated thermal conductance across the Si-PS interface as a function of the grafting density for four SAM molecules, with error bars denoting the standard deviation. To explore how the grafted densities act on the ITC, each SAM molecule was first grafted with the number increasing from 0 to 1, 2, 4, 8, 16, and 32, corresponding to the grafted density of 0.053, 0.106, 0.212, 0.424, 0.848, and 1.696 chains nm⁻², respectively. Obviously, the ITC increases with the increasing density of grafted chains for each SAMs. The rising-rate is almost remained unchanged before the density of the graded SAMs took 0.424 chains nm⁻²; afterwards, the rising rate gradually decreased with the increasing density, and a plateau was expected. Previous studies

concerning the grafting density of SAM molecules, such as the graphene-PMMA interface [29], have explored how the grafting density affects the ITC. Therefore, we will focus on how the ITC can be further strengthened by grafting the different SAM molecules where they have the same grafted density. To clearly illustrate the effect of different SAMs on ITC, the decorated SAMs having the grafting density of $1.696 \text{ chains nm}^{-2}$ are chosen to understand how different SAMs work on the heat transfer mechanism across the Si-PS interface due to their highest ITC values as follows. The ITC across the undecorated Si-PS interface is found to be $52.18 \text{ MW m}^{-2} \text{ K}^{-1}$, significantly lower than the other four SAM-decorated interfaces. Focusing on four SAMs-functionalized interfaces, ITC is improved to various degrees. Ranking from the lowest improvement to the highest are APTMS, MPTMS, nBTMS, and CPTMS. By comparison with the pristine Si-PS interface, four SAMs-decorated interfaces show the ITC improved by 264.46%, 310.51%, 408.38%, and 507.02%, respectively, i.e., from 52.18 to 190.17, 214.19, 265.26 and $316.73 \text{ MW m}^{-2} \text{ K}^{-1}$. Notably, all four SAM molecules only have different end groups. Carried by molecular SAMs that introduce into the PS polymer matrix, the different interaction between SAM molecules and PS substantially boosts the interface's bonding strength, leading to improved ITC.

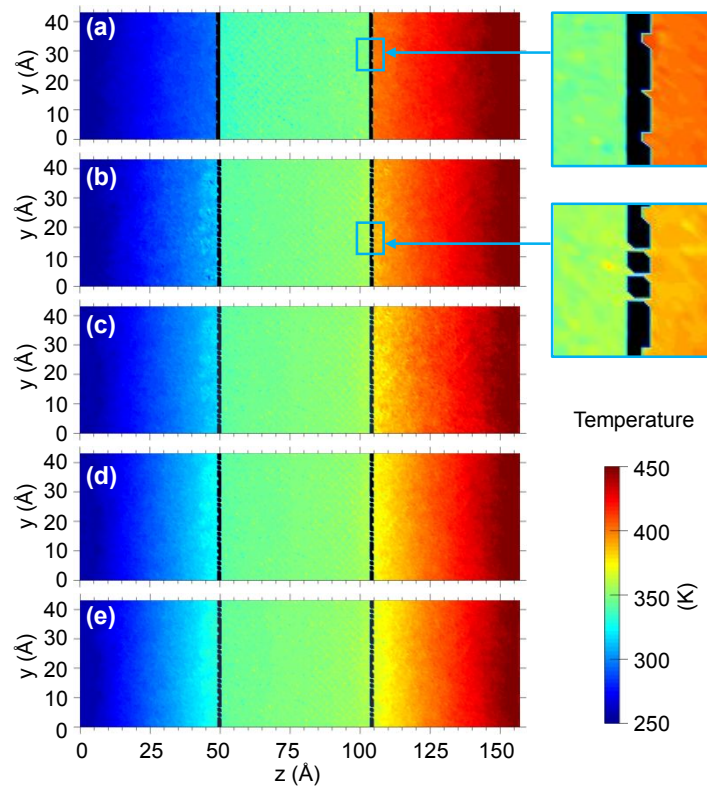


Fig. 3. Temperature distribution contours of five decorative systems: (a) Si-PS, (b) Si: APTMS-PS, (c) Si: MPTMS-PS, (d) Si: nBTMS-PS and (e) Si: CPTMS-PS. The black belts denote the zero-temperature area occupied by no atoms.

3.3. Temperature Distribution Field

Interfaces decorated with molecular SAMs mitigate the spatial discontinuities where Si contracts with PS within the temperature contours, consequently facilitating interfacial heat conduction. **Fig. 3** displays the temperature distribution field calculated by imposing the same temperature at the sink and source regions for systems without and with the four SAMs. The black ribbons in **Fig. 3a** indicate that the pristine Si-PS interface has a strong discontinuity, which suggests that no atoms move through these areas because of the steric repulsion. A comparison shows that discontinuity is partially eliminated when interfaces decorate with SAM molecules. **Fig. 3b-e** illustrates that those black ribbons are divided into several pieces at the location where SAMs

are there and are slightly thinner. The partially removed discontinuity indicates that the incorporated molecular SAMs provide new heat transfer pathways for more effective thermal transport at the Si-PS interface.

More importantly, the hybrid region developed by molecular SAMs and PS has higher thermal conductivities. On the contrary, the pristine Si-PS interface gives a higher temperature fall than other interfaces decorated with molecular SAMs, demonstrating the ineffective heat transport across the Si-PS interface, corresponding to the calculations shown in **Fig. 2**. In addition, in **Fig. S5a-e**, the mixed SAM-PS region has lower temperature gradients, resulting in higher thermal conductivities than those regions only consisting of PS. The enhanced thermal conductivities within the blending region can be understood from two aspects. On one side, the strong non-bonded interactions between PS and the molecular SAMs, including APTMS, MPTMS, nBTMS, and CPTMS, are formed. Like some previous studies [28], such as H-bonds, the strong non-bonded interactions can provide thermal bridges between SAMs and PS and enhance heat transfer within the blending region. On the other side, the morphology of the grafted molecular SAMs is more prolonged in the mixing region. Previous studies indicated that the stretched molecular chains should have higher thermal conductivities than their amorphous counterparts [63, 64]. On the basis of both aspects mentioned above, heat transfer should be delivered more efficiently in the mixed SAM-PS region.

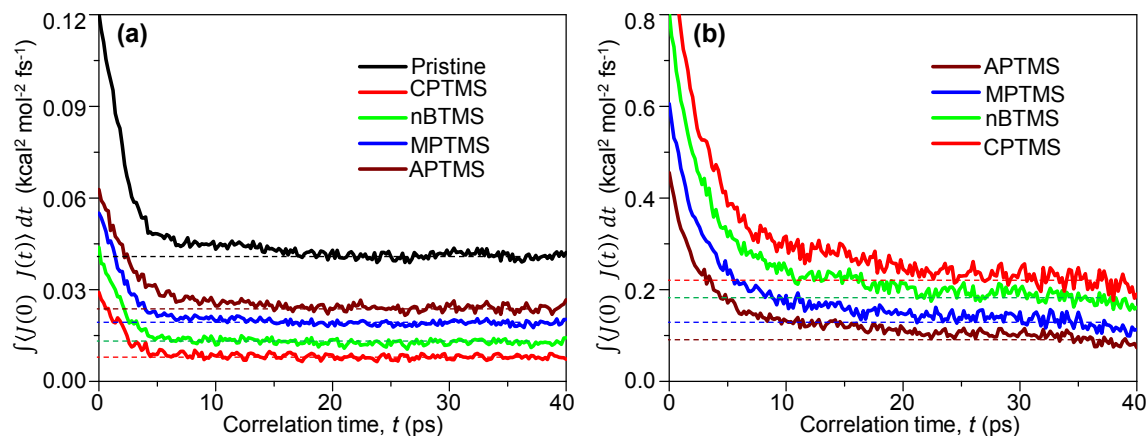


Fig. 4. The integrated autocorrelation of the exchanged heat flux across interfaces (a) between Si and PS, and (b) between PS and molecular SAMs for systems functionalized with four molecules, such as APTMS, MPTMS, nBTMS, and CPTMS. Dashed lines represent the convergence of the integrated autocorrelation function.

3.4. Integrated Autocorrelation of Heat Flux across Si-PS interface

To quantitatively describe how heat flux exchanges across the Si-PS interface, we analyze the integrated autocorrelation of heat flux when energy transfers through a specific path or a particular atomic group. Adding up all the contributions from different heat transfer paths will obtain the ITC. **Fig. 4a** displays the integrated autocorrelation function of the interfacial heat flux for four decoration systems, while **Fig. 4b** shows that between PS and molecular SAMs in the same system. With the correlation time increasing, all curves first decrease and then eventually converge to a plateau. The dashed line shown in **Fig 4** represents the converged value. On one hand, compared to the pristine Si-PS interface, **Fig. 4a** shows that the Si-PS interface decorated with the four molecular SAMs shows a dramatically decreasing energy transfer through the Si \rightarrow PS path. This comes because of the grafted SAMs, which cut down the contact area between Si and PS polymer, leading to a reduced energy transfer in this path due to the existing SAMs. On the other hand, when the Si-PS interface is functionalized by the four molecular SAMs, **Fig. 4a**

indicates that the Si-PS interface decorated with APTMS has a higher energy transfer, followed by MPTMS, nBTMS, and CPTMS. Although the grafted SAMs have almost the same contact area across the Si-PS interface, the totally different end functional group of the grafted SAMs gives the non-bonded interactions in different intensities. The stronger non-bonded interactions can further strengthen the local compactness of PS polymer, which allows more energy to arrive at the interface and exchange the energy across the interface via the SAMs \rightarrow PS path.

In addition, **Fig. 4b** shows that the energy exchanged through the SAMs \rightarrow PS route is much more than that transferred through the Si \rightarrow PS route. Energy transfer is the highest for the Si-PS interface decorated with CPTMS, followed by nBTMS, MPTMS, and APTMS. This physical understanding is quite easy. The different end groups of the grafted SAMs produce different non-bonded interactions between SAMs and PS polymer. The stronger non-bonded interactions lead to a higher transfer efficiency of energy. Importantly, the results also echo the investigation from **Fig. 4** that energy transfer between PS and SAMs is more effective than that between Si and PS. Both investigations indicate that the extended molecular SAMs could be considered as efficient linkers to mediate two dissimilar materials, e.g., between Si and PS, and the grafted SAMs with different groups at the end can further tailor the heat transfer across the interface.

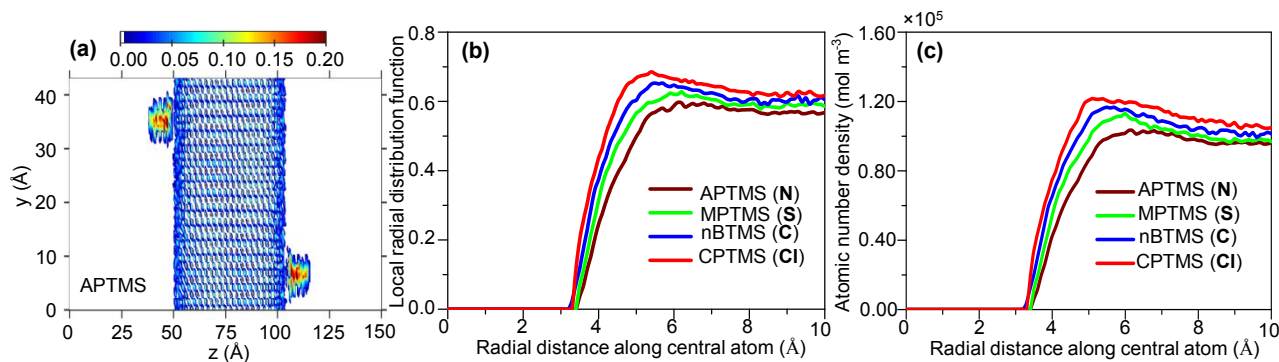


Fig. 5. (a) Atomic density profiles of molecular SAMs for Si: APTMS-PS system. One molecular chain at each Si side is chosen as the representative chain. (b-c) The local RDF and the local atomic density versus the radial distance along with the reference atom for four molecular SAM-decorated systems, respectively. The letter in the brackets, including N, S, C, and Cl, corresponds to the reference atom in each SAM molecule.

3.5. Uprise Molecular Morphology and Density Distribution

To illustrate SAM molecules' uprise within the PS matrix, **Fig.5a** and **Fig. S6a-c** displays the atomic density distributions related to Si and functionalized SAM molecules. Here, one SAM molecule is chosen at each Si block side. The grafted SAM molecules, including APTMS, MPTMS, nBTMS, and CPTMS, show the uprisen configurations. Such extended configurations are partially because of their steric repulsions between the SAM molecules and the limited backbone length of the SAMs, which imposes the molecules to be relatively straight. Moreover, the strong non-bonded interactions between the end group and PS further strengthen such configurations. The extended molecular morphology of SAMs further enhances the ITC since it can force the heat energy to be transferred along molecular chains where heat conduction is more effective.

To further understand the different non-bonded interactions between PS and SAMs, **Fig.5b** plots the local RDF versus the radial distance around the reference atom for the four systems with SAMs. Here, because all molecular SAMs have the same backbone but different functional groups at the end, the dominant atom of the functional group is selected as the reference atom. For example,

N, S, C, and Cl atoms are chosen as the reference atoms for APTMS, MPTMS, nBTMS, and CPTMS molecules, respectively. All these local radial distribution functions rise first, then reduce, and finally tend to an upper limit with the increasing radial distance. Within the same radial distance, the CPTMS-functionalized interface has the highest probability of existing in an atom away from the reference atom when the radial distance is smaller than 8 Å, followed by nBTMS, MPTMS, and APTMS. However, when the radial distance is larger than 8 Å, the functional group has a minimal impact on the PS polymers, almost leading to the same probability. In addition to that, **Fig.5c** plots the relationship between the local atomic density and the radial distance around the same reference atom for four systems decorated with SAMs. Results show that the CPTMS-functionalized interface has the largest atomic number density along with the radial distance away from the reference atom, followed by nBTMS, MPTMS, and APTMS. These investigations indicate that non-bonded interactions between CPTMS and PS polymer are the strongest within a certain radial distance, followed by nBTMS, MPTMS, and APTMS. When the radial distance away from the reference atom exceeds a certain distance, SAM molecules are less attractive to PS polymer due to the weak non-bonded interaction caused by the distance limit.

Table 1 Attraction constants for five functional groups

Groups	G_{di} ($J^{0.5}mol^{-1}cm^{1.5}$)	G_{pi} ($J^{0.5}mol^{-1}cm^{1.5}$)	G_{hi} ($J^{0.5}mol^{-1}cm^{1.5}$)
-NH ₂	280	0	8400
-SH	645.1	0	0
-CH ₃	420	0	0
-CH ₂ -	270	0	0
-Cl	450	550	400

3.6. Affinity Energy between SAMs and PS polymer

Fig 6 has indicated that SAMs can both improve the interfacial adhesion and ITC between inorganic-organic interfaces, which agrees well with some previous studies [26, 65, 66]. It also indicates that the enhanced interface bonding strength improves the ITC, which is in line with molecular SAMs-grafted metal-inorganic interfaces [65, 67]. To further analyze how compact the molecular bonding strength is on the interface, we calculate the mixing affinity energy, Chi parameter, and solubility parameters of PS and SAMs. The parameters employed to analyze their solubility parameters are shown in **Table 1** [68]. **Fig 6a-b** plots the mixing affinity energy and Chi parameter as a function of the grafted SAMs. Based on the physical understanding, the larger Chi parameter and higher mixing affinity energy indicate less miscibility between SAMs and PS.

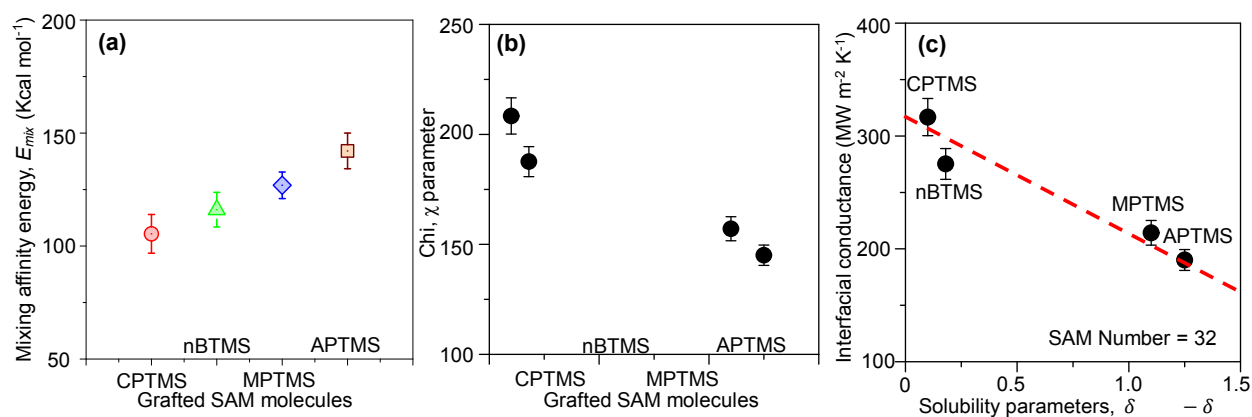


Fig. 6. Compatibility metrics of (a) mixing affinity energy, E_{mix} and (b) Chi parameter, χ between PS and molecular SAMs. (c) Relationship between thermal conductance across Si-PS interfaces and difference in solubility parameters, $\delta_{silane} - \delta_{PS}$.

Results show that CPTMS has both the lowest mixing affinity and Chi parameter, followed by nBTMS, MPTMS, and APTMS, which demonstrates that the CPTMS molecule is easily miscible with PS polymer. In other words, CPTMS can easily attract PS polymer, and energy can be transferred faster through CPTMS molecules. In addition to that, we directly calculate the solubility parameters, which can describe how well-compatible two materials are. **Fig 6c** plots the ITC as a function of solubility parameters of different SAM molecules. In general, two distinct

materials giving similar solubility parameters can be treated as more compatible, suggesting their favorable contacts or soluble. Results show that when SAM molecules change from APTMS to MPTMS, nBTMS, and CPTMS, the ITC almost increases linearly with the decreased discrepancy of solubility parameters. All these investigations indicate that the more compatible SAM molecule can lead to favorable contact with PS polymer and facilitate the energy transfer vis the SAM \rightarrow Si path.

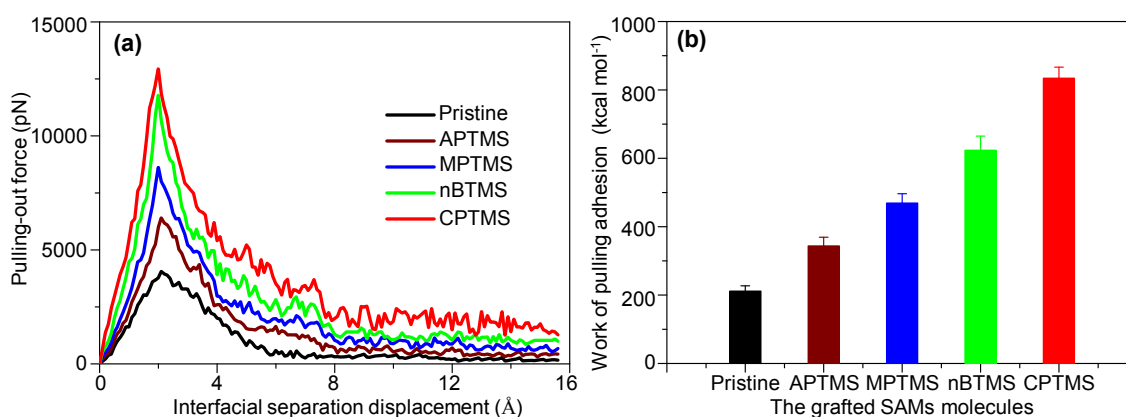


Fig. 7. (a) Relationship between the applied pullout force and the interfacial separation displacement for the pristine system and four SAMs-based decorative systems, including APTMS, MPTMS, nBTMS, and CPTMS. (b) The calculated work of the pulling-out force by integrating the pulling-out force-displacement curves for the pristine system and four SAMs-based decorative systems.

3.7. Interfacial Bonding Strength

Previous experiments and MD simulations on the solid-liquid and solid-solid interface have demonstrated that the ITC is directly related to the interfacial bonding strength [69, 70]. **Fig 7a** presents the relationship between the pullout force and the interfacial separation distance when separating molecular SAMs-decorated Si-PS interfaces. The peak points located in force-displacement curves denote the maximum pulling forces employed to separate pristine or

decorative interfaces, which also represents the failure strength. These investigations show that, on one side, when the SAM chains are grafted to the Si surface, the interfacial strength is boosted, and a longer time is required to pull out due to the interaction between the embedded SAMs and PS polymer; on the other side, when Si-PS interface is decorated with different SAMs, interface functionalized with CPTMS has a stronger interfacial bonding strength, and the pullout requires much more time to achieve due to the strong non-bonded interactions between the molecular SAMs and PS caused by $-Cl$ functional groups. In other words, mechanically, both the interfacial failure and separation strength contribute to the total work of bonding strength around the interface, which is shown in **Fig 7b** for the different systems under investigation. After the Si-PS interface is decorated with different molecular SAMs, the CPTMS-functionalized interface requires more work to complete the separation. This is also in agreement with the finding in **Fig 7** that an interface grafted with different SAMs leads to different ITC, and the CPTMS-functionalized interface has the highest ITC, followed by nBTMS, MPTMS, and APTMS.

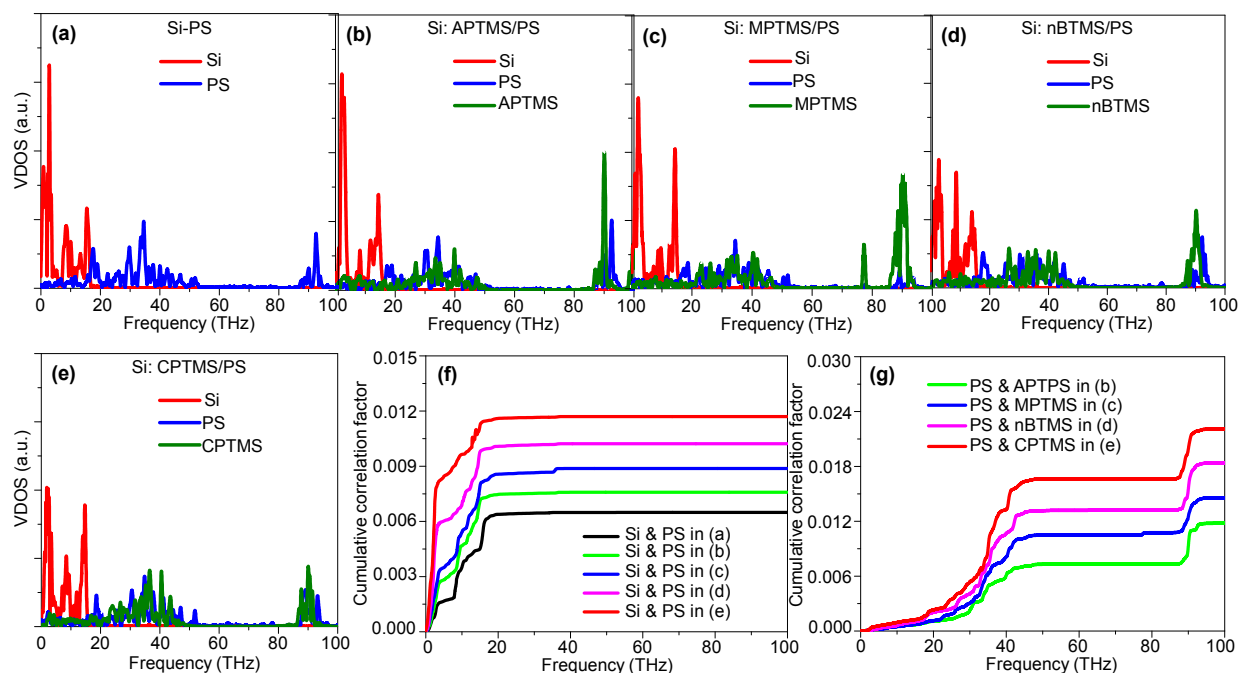


Fig. 8. VDOS for different compositions in (a) Si-PS, (b) Si: APTMS-PS, (c) Si: MPTMS-PS, (d) Si: nBTMS-PS and (e) Si: CPTMS-PS. (f) The cumulative correlation factor, M , between Si and PS for the pristine and four decorative systems. (g) The M between molecular SAMs and PS for the four molecular SAM-decorated systems.

3.8. *Vibrational Spectra Coupling*

SAM molecules facilitate the interfacial thermal transfer as a vibrational modulator that regulates the coupled vibration between Si and PS. Based on both the diffusive and acoustic mismatch theory [39], the ITC has a strong correlation with the coupled vibration spectra between two materials producing an interface [71-73]. Studies have indicated that vibration modes between two materials have a better match, leading to higher thermal conductance across interfaces [74]. **Fig.8a-e** displays the VDOS for all decorative systems developing five types of interfaces. Without SAMs decoration, the Si-PS cumulative correlation factor shown in **Fig.8f** indicates that the pristine Si-PS interface emerges the poor vibrational coupling. The poorly coupled vibration between Si and PS well echoes the corresponding mismatch illustrated in **Fig.8a**, where PS reveals frequency peaks around 33.69 THz and 88.62 THz while Si reveals frequency peaks ranging from 0 to 20 THz. By assembling SAMs, the Si vibration is drastically weakened (**Fig.8b-e**) at the interface, and the vibrational match is obviously strengthened between SAMs and PS. For instance, with regard to the Si: CPTMS-PS interface (**Fig.8e**), many overlapped peaks between PS and CPTMS are observed at the considered frequency range. The enhanced vibrational match for SAM-decorated systems is also investigated in **Fig.8f**, where all molecular SAM-functionalized interfaces provide a stronger correlation compared to the pristine Si-PS interface, and the Si: CPTMS-PS interface with the strongest non-bonded interaction owns the strongest interface correlation. Similar rankings are also observed from the vibration coupling effect between PS and SAMs molecules, as shown in **Fig.8g**.

4. Conclusions

In this study, we demonstrate that the interface between Si and PS decorated by molecular SAMs exhibits significantly different ITC, which has a broad range of applications in heat removal and thermal management of electronic devices. Compared with the pristine Si-PS interface, molecular SAMs-bonded interfaces, including Si: APTMS-PS, Si: MPTMS-PS, Si: Nbtms-PS, and Si: CPTMS-PS give a substantial improvement of ITC by 264.46%, 310.51%, 408.38%, and 507.02%, respectively. Obviously, the unique end functional groups carried by SAMs offer the key contributions to remarkably modulating the thermal conduction across Si-PS interfaces. Such difference greatly depends on the different non-bonded interactions and compatibility between PS and SAMs. For instance, the Si-CPTMS-PS interface features the strongest non-bonded interactions and highest compatibility, $-Cl \cdots PS$, leads to the ITC 507.02% more than the pristine interface. The anomalous improvement for all molecular SAMs-decorated interfaces is attributed to four dominated factors: (1) the stretched and well-aligned molecular chains in the SAM-PS blending domain, (2) the strong vibration coupling between PS and SAMs, (3) the developed thermal bridges between Si and molecular SAMs, (4) the strong non-bonded interactions between SAMs molecules and PS. All these factors contribute to making the thermal transfer between two dissimilar materials more efficient. The proposed molecular decorating strategy is expected to offer a fundamental understanding of molecular SAMs-functionalized interfacial engineering for strengthening multi-material system's thermal management, including the polymer-semiconductor composites.

Notes

The authors declare no competing financial interest.

Acknowledgement

Y.L. gratefully acknowledges financial support from the U.S. National Science Foundation (CMMI-1762661, CMMI-1934829 and CAREER Award CMMI-2046751) and 3M's Non-Tenured Faculty Award. Any opinion, findings, and conclusions or recommendations expressed in this material are those of the authors and do not necessarily reflect the views of the U.S. National Science Foundation. This research also benefited in part from the computational resources and staff contributions provided by the Booth Engineering Center for Advanced Technology (BECAT) at the University of Connecticut. The authors also acknowledge the Texas Advanced Computing Center (TACC) at The University of Texas at Austin (Frontera project and National Science Foundation Award 1818253) and National Renewable Energy Laboratory (Eagle Computing System) for providing HPC resources that have contributed to the research results reported within this paper.

References

- [1] A.L. Moore, L. Shi, Emerging challenges and materials for thermal management of electronics, *Materials today*. 17(4) (2014) 163-174.
- [2] E. Pop, Energy dissipation and transport in nanoscale devices, *Nano Research*. 3(3) (2010) 147-169.
- [3] P. Zhang, P. Yuan, X. Jiang, S. Zhai, J. Zeng, Y. Xian, H. Qin, D. Yang, A theoretical review on interfacial thermal transport at the nanoscale, *Small*. 14(2) (2018) 1702769.
- [4] G. Cuniberti, G. Fagas, K. Richter, Introducing molecular electronics: A brief overview, *Introducing Molecular Electronics*. (2006) 1-10.
- [5] K. Ruan, X. Shi, Y. Guo, J. Gu, Interfacial thermal resistance in thermally conductive polymer composites: a review, *Composites Communications*. 22 (2020) 100518.
- [6] C. Fu, Q. Li, J. Lu, S. Mateti, Q. Cai, X. Zeng, G. Du, R. Sun, Y. Chen, J. Xu, Improving thermal conductivity of polymer composites by reducing interfacial thermal resistance between boron nitride nanotubes, *Composites Science and Technology*. 165 (2018) 322-330.
- [7] D. An, S. Cheng, S. Xi, Z. Zhang, X. Duan, Y. Ren, J. Li, Z. Sun, Y. Liu, C.-P. Wong, Flexible thermal interfacial materials with covalent bond connections for improving high thermal conductivity, *Chemical Engineering Journal*. 383 (2020) 123151.
- [8] M. Caccia, A. Rodríguez, J. Narciso, Diamond surface modification to enhance interfacial thermal conductivity in Al/diamond composites, *Jom*. 66(6) (2014) 920-925.
- [9] E. Easy, Y. Gao, Y. Wang, D. Yan, S.M. Gousheghir, E.-H. Yang, B. Xu, X. Zhang, Experimental and Computational Investigation of Layer-Dependent Thermal Conductivities and Interfacial Thermal Conductance of One- to Three-Layer WSe₂, *ACS Appl. Mater. Interfaces*. 13(11) (2021) 13063-13071.
- [10] J. Chen, Advanced electron microscopy of nanophased synthetic polymers and soft complexes for energy and medicine applications, *Nanomaterials*. 11(9) (2021) 2405.

- [11] H. Ma, B. Gao, M. Wang, Z. Yuan, J. Shen, J. Zhao, Y. Feng, Strategies for enhancing thermal conductivity of polymer-based thermal interface materials: A review, *Journal of Materials Science*. 56(2) (2021) 1064-1086.
- [12] S. Jasmee, G. Omar, S.S.C. Othaman, N.A. Masripan, H. A. Hamid, Interface thermal resistance and thermal conductivity of polymer composites at different types, shapes, and sizes of fillers: A review, *Polymer Composites*. 42(6) (2021) 2629-2652.
- [13] P.E. Hopkins, M. Baraket, E.V. Barnat, T.E. Beechem, S.P. Kearney, J.C. Duda, J.T. Robinson, S.G. Walton, Manipulating thermal conductance at metal-graphene contacts via chemical functionalization, *Nano letters*. 12(2) (2012) 590-595.
- [14] J.C. Duda, P.E. Hopkins, Systematically controlling Kapitza conductance via chemical etching, *Applied Physics Letters*. 100(11) (2012) 111602.
- [15] Q. Liu, Y. Gao, B. Xu, Transferable, Deep-Learning-Driven Fast Prediction and Design of Thermal Transport in Mechanically Stretched Graphene Flakes, *ACS Nano*. 15(10) (2021) 16597-16606.
- [16] Y. Wang, Y. Cao, K. Zhou, Z. Xu, Assessment of Self - Assembled Monolayers as High - Performance Thermal Interface Materials, *Advanced Materials Interfaces*. 4(15) (2017) 1700355.
- [17] Z. Tian, A. Marconnet, G. Chen, Enhancing solid-liquid interface thermal transport using self-assembled monolayers, *Applied Physics Letters*. 106(21) (2015) 211602.
- [18] J. He, L. Zhang, L. Liu, Improving thermal conduction across cathode/electrolyte interfaces in solid-state lithium-ion batteries by hierarchical hydrogen-bond network, *Materials & Design*. 194 (2020) 108927.
- [19] D. Huang, R. Ma, T. Zhang, T. Luo, Origin of Hydrophilic Surface Functionalization-Induced Thermal Conductance Enhancement across Solid-Water Interfaces, *ACS Appl. Mater. Interfaces*. 10(33) (2018) 28159-28165.
- [20] C. Yuan, M. Huang, Y. Cheng, X. Luo, Bonding-induced thermal transport enhancement across a hard/soft material interface using molecular monolayers, *Physical Chemistry Chemical Physics*. 19(10) (2017) 7352-7358.
- [21] E. Ruckenstein, Z. Li, Surface modification and functionalization through the self-assembled monolayer and graft polymerization, *Advances in Colloid and Interface Science*. 113(1) (2005) 43-63.
- [22] S. Park, H.J. Yoon, Thermal and Thermoelectric Properties of SAM-Based Molecular Junctions, *ACS Applied Materials & Interfaces*. (2021).
- [23] S. Tian, D. Huang, Z. Xu, S. Wu, T. Luo, G. Xiong, Enhanced thermal transport across the interface between charged graphene and poly(ethylene oxide) by non-covalent functionalization, *Int. J. Heat Mass Transfer*. 183 (2022) 122188.
- [24] S. Tian, Z. Xu, S. Wu, T. Luo, G. Xiong, Anisotropically tuning interfacial thermal conductance between graphite and poly(ethylene oxide) by lithium-ion intercalation: A molecular dynamics study, *Int. J. Heat Mass Transfer*. 195 (2022) 123134.
- [25] L. Song, Y. Zhang, W. Yang, J. Tan, L. Cheng, Molecular Structure Effect of a Self-Assembled Monolayer on Thermal Resistance across an Interface, *Polymers*. 13(21) (2021) 3732.
- [26] K. Zheng, F. Sun, J. Zhu, Y. Ma, X. Li, D. Tang, F. Wang, X. Wang, Enhancing the Thermal Conductance of Polymer and Sapphire Interface via Self-Assembled Monolayer, *ACS Nano*. 10(8) (2016) 7792-7798.
- [27] T. Zhang, A.R. Gans-Forrest, E. Lee, X. Zhang, C. Qu, Y. Pang, F. Sun, T. Luo, Role of hydrogen bonds in thermal transport across hard/soft material interfaces, *ACS applied materials & interfaces*. 8(48) (2016) 33326-33334.
- [28] L. Zhang, L. Liu, Hierarchically hydrogen-bonded graphene/polymer interfaces with drastically enhanced interfacial thermal conductance, *Nanoscale*. 11(8) (2019) 3656-3664.
- [29] L. Zhang, L. Liu, Polymeric Self-Assembled Monolayers Anomalously Improve Thermal Transport across Graphene/Polymer Interfaces, *ACS Appl. Mater. Interfaces*. 9(34) (2017) 28949-28958.
- [30] J. Lu, K. Yuan, F. Sun, K. Zheng, Z. Zhang, J. Zhu, X. Wang, X. Zhang, Y. Zhuang, Y. Ma, Self-assembled monolayers for the polymer/semiconductor interface with improved interfacial thermal management, *ACS applied materials & interfaces*. 11(45) (2019) 42708-42714.

- [31] K.M. Stocker, J.D. Gezelter, Simulations of heat conduction at thiolate-capped gold surfaces: the role of chain length and solvent penetration, *The Journal of Physical Chemistry C*. 117(15) (2013) 7605-7612.
- [32] F. Sun, T. Zhang, M.M. Jobbins, Z. Guo, X. Zhang, Z. Zheng, D. Tang, S. Ptasinska, T. Luo, Molecular Bridge Enables Anomalous Enhancement in Thermal Transport across Hard-Soft Material Interfaces, *Adv. Mater.* 26(35) (2014) 6093-6099.
- [33] F. Sun, T. Zhang, M.M. Jobbins, Z. Guo, X. Zhang, Z. Zheng, D. Tang, S. Ptasinska, T. Luo, Molecular Bridge Enables Anomalous Enhancement in Thermal Transport across Hard - Soft Material Interfaces, *Advanced Materials*. 26(35) (2014) 6093-6099.
- [34] G.F. Lawler, A self-avoiding random walk, *Duke Mathematical Journal*. 47(3) (1980) 655-693.
- [35] W. Humphrey, A. Dalke, K. Schulten, VMD: Visual molecular dynamics, *J. Mol. Graph.* 14(1) (1996) 33-38.
- [36] H. Kim, A.A. Abdala, C.W. Macosko, Graphene/Polymer Nanocomposites, *Macromolecules*. 43(16) (2010) 6515-6530.
- [37] M. Shen, W.J. Evans, D. Cahill, P. Keblinski, Bonding and pressure-tunable interfacial thermal conductance, *Phys. Rev. B*. 84(19) (2011) 195432.
- [38] S. Majumdar, J.A. Malen, A.J.H. McGaughey, Cooperative Molecular Behavior Enhances the Thermal Conductance of Binary Self-Assembled Monolayer Junctions, *Nano Lett.* 17(1) (2017) 220-227.
- [39] J. Severin, P. Jund, Thermal conductivity calculation in anisotropic crystals by molecular dynamics: Application to α -Fe₂O₃, *J. Chem. Phys.* 146(5) (2017) 054505.
- [40] S. Plimpton, Fast Parallel Algorithms for Short-Range Molecular Dynamics, *Journal of Computational Physics*. 117(1) (1995) 1-19.
- [41] J. Tersoff, New empirical approach for the structure and energy of covalent systems, *Phys. Rev. B*. 37(12) (1988) 6991-7000.
- [42] W.L. Jorgensen, D.S. Maxwell, J. Tirado-Rives, Development and Testing of the OPLS All-Atom Force Field on Conformational Energetics and Properties of Organic Liquids, *J. Am. Chem. Soc.* 118(45) (1996) 11225-11236.
- [43] M.L.P. Price, D. Ostrovsky, W.L. Jorgensen, Gas-phase and liquid-state properties of esters, nitriles, and nitro compounds with the OPLS-AA force field, *J. Comput. Chem.* 22(13) (2001) 1340-1352.
- [44] R. Godawat, S.N. Jamadagni, S. Garde, Characterizing hydrophobicity of interfaces by using cavity formation, solute binding, and water correlations, *Proceedings of the National Academy of Sciences*. 106(36) (2009) 15119.
- [45] S. Kuang, J.D. Gezelter, Simulating Interfacial Thermal Conductance at Metal-Solvent Interfaces: The Role of Chemical Capping Agents, *The Journal of Physical Chemistry C*. 115(45) (2011) 22475-22483.
- [46] A.K. Rappe, C.J. Casewit, K.S. Colwell, W.A. Goddard, W.M. Skiff, UFF, a full periodic table force field for molecular mechanics and molecular dynamics simulations, *J. Am. Chem. Soc.* 114(25) (1992) 10024-10035.
- [47] F. Müller-Plathe, A simple nonequilibrium molecular dynamics method for calculating the thermal conductivity, *J. Chem. Phys.* 106(14) (1997) 6082-6085.
- [48] M. Zhang, E. Lussetti, L.E. de Souza, F. Müller-Plathe, Thermal conductivities of molecular liquids by reverse nonequilibrium molecular dynamics, *J. Phys. Chem. B*. 109(31) (2005) 15060-15067.
- [49] P. Boone, H. Babaei, C.E. Wilmer, Heat Flux for Many-Body Interactions: Corrections to LAMMPS, *J. Chem. Theory Comput.* 15(10) (2019) 5579-5587.
- [50] C.F. Fan, B.D. Olafson, M. Blanco, S.L. Hsu, Application of molecular simulation to derive phase diagrams of binary mixtures, *Macromolecules*. 25(14) (1992) 3667-3676.
- [51] K.S. Schweizer, Microscopic theory of the dynamics of polymeric liquids: General formulation of a mode - mode - coupling approach, *J. Chem. Phys.* 91(9) (1989) 5802-5821.
- [52] B. Li, J. Lan, L. Wang, Interface Thermal Resistance between Dissimilar Anharmonic Lattices, *Phys. Rev. Lett.* 95(10) (2005) 104302.
- [53] Y. Weng, F. Delgado, S. Son, T. Burg, S. Wasserman, S. Manalis, Mass sensors with mechanical traps for weighing single cells in different fluids, *Lab Chip*. 11 (2011) 4174-80.

- [54] X. Wang, P. Wu, Preparation of Highly Thermally Conductive Polymer Composite at Low Filler Content via a Self-Assembly Process between Polystyrene Microspheres and Boron Nitride Nanosheets, *ACS Appl. Mater. Interfaces*. 9(23) (2017) 19934-19944.
- [55] I.-L. Ngo, S. Jeon, C. Byon, Thermal conductivity of transparent and flexible polymers containing fillers: A literature review, *Int. J. Heat Mass Transfer*. 98 (2016) 219-226.
- [56] C.J. Glassbrenner, G.A. Slack, Thermal Conductivity of Silicon and Germanium from 3\ifmmode^\circ\else\textdegree\fi K to the Melting Point, *Physical Review*. 134(4A) (1964) A1058-A1069.
- [57] M. Kazan, G. Guisbiers, S. Pereira, M.R. Correia, P. Masri, A. Bruyant, S. Volz, P. Royer, Thermal conductivity of silicon bulk and nanowires: Effects of isotopic composition, phonon confinement, and surface roughness, *J. Appl. Phys.* 107(8) (2010) 083503.
- [58] C. Jeong, S. Datta, M. Lundstrom, Thermal conductivity of bulk and thin-film silicon: A Landauer approach, *J. Appl. Phys.* 111(9) (2012) 093708.
- [59] K. Zheng, F. Sun, X. Tian, J. Zhu, Y. Ma, D. Tang, F. Wang, Tuning the Interfacial Thermal Conductance between Polystyrene and Sapphire by Controlling the Interfacial Adhesion, *ACS Appl. Mater. Interfaces*. 7(42) (2015) 23644-23649.
- [60] K. Zheng, J. Zhu, M. Yong-Mei, W. Fo-Song, Interfacial thermal resistance between high-density polyethylene (HDPE) and sapphire, *Chin. Phys. B*. 23 (2014) 107307.
- [61] J. Liu, S. Ju, Y. Ding, R. Yang, Size effect on the thermal conductivity of ultrathin polystyrene films, *Appl. Phys. Lett.* 104(15) (2014) 153110.
- [62] M. Hu, S. Shenogin, P. Keblinski, Molecular dynamics simulation of interfacial thermal conductance between silicon and amorphous polyethylene, *Appl. Phys. Lett.* 91(24) (2007) 241910.
- [63] A. Henry, G. Chen, High Thermal Conductivity of Single Polyethylene Chains Using Molecular Dynamics Simulations, *Physical Review Letters*. 101(23) (2008) 235502.
- [64] Z. Wang, J.A. Carter, A. Lagutchev, Y.K. Koh, N.-H. Seong, D.G. Cahill, D.D. Dlott, Ultrafast Flash Thermal Conductance of Molecular Chains, *Science*. 317(5839) (2007) 787.
- [65] M.D. Losego, M.E. Grady, N.R. Sottos, D.G. Cahill, P.V. Braun, Effects of chemical bonding on heat transport across interfaces, *Nat. Mater.* 11(6) (2012) 502-506.
- [66] J. Choi, S.B. Cho, B.S. Lee, Y.K. Joung, K. Park, D.K. Han, Improvement of Interfacial Adhesion of Biodegradable Polymers Coated on Metal Surface by Nanocoupling, *Langmuir*. 27(23) (2011) 14232-14239.
- [67] P.J. O'Brien, S. Shenogin, J. Liu, P.K. Chow, D. Laurencin, P.H. Mutin, M. Yamaguchi, P. Keblinski, G. Ramanath, Bonding-induced thermal conductance enhancement at inorganic heterointerfaces using nanomolecular monolayers, *Nat. Mater.* 12(2) (2013) 118-122.
- [68] C.M. Hansen, The Universality of the Solubility Parameter, *Product R&D*. 8(1) (1969) 2-11.
- [69] N. Shenogina, R. Godawat, P. Keblinski, S. Garde, How Wetting and Adhesion Affect Thermal Conductance of a Range of Hydrophobic to Hydrophilic Aqueous Interfaces, *Phys. Rev. Lett.* 102(15) (2009) 156101.
- [70] B. Ramos-Alvarado, S. Kumar, G.P. Peterson, Solid-Liquid Thermal Transport and Its Relationship with Wettability and the Interfacial Liquid Structure, *The Journal of Physical Chemistry Letters*. 7(17) (2016) 3497-3501.
- [71] S. Lin, M.J. Buehler, The effect of non-covalent functionalization on the thermal conductance of graphene/organic interfaces, *Nanotechnology*. 24(16) (2013) 165702.
- [72] Y. Wang, C. Yang, Q.-X. Pei, Y. Zhang, Some Aspects of Thermal Transport across the Interface between Graphene and Epoxy in Nanocomposites, *ACS Appl. Mater. Interfaces*. 8(12) (2016) 8272-8279.
- [73] Y. Wang, H.F. Zhan, Y. Xiang, C. Yang, C.M. Wang, Y.Y. Zhang, Effect of Covalent Functionalization on Thermal Transport across Graphene-Polymer Interfaces, *The Journal of Physical Chemistry C*. 119(22) (2015) 12731-12738.

[74] D.G. Cahill, P.V. Braun, G. Chen, D.R. Clarke, S. Fan, K.E. Goodson, P. Keblinski, W.P. King, G.D. Mahan, A. Majumdar, H.J. Maris, S.R. Phillpot, E. Pop, L. Shi, Nanoscale thermal transport. II. 2003–2012, *Appl. Phys. Rev.* 1(1) (2014) 011305.